

## Article

# Modelling and Prediction of Process Parameters with Low Energy Consumption in Wire Arc Additive Manufacturing Based on Machine Learning

Haitao Zhang <sup>1</sup>, Xingwang Bai <sup>1,\*</sup>, Honghui Dong <sup>1</sup> and Haiou Zhang <sup>2</sup>

<sup>1</sup> School of Mechanical Engineering, University of South China, Hengyang 421001, China; htzhang07@163.com (H.Z.)

<sup>2</sup> School of Mechanical Science and Engineering, Huazhong University of Science and Technology, Wuhan 430074, China

\* Correspondence: pancard@126.com

**Abstract:** Wire arc additive manufacturing (WAAM) has attracted increasing interest in industry and academia due to its capability to produce large and complex metallic components at a high deposition rate. One of the basic tasks in WAAM is to determine appropriate process parameters, which will directly affect the morphology and quality of the weld bead. However, the selection of process parameters relies heavily on empirical data from trial-and-error experiments, which results in significant time and cost expenditures. This paper employed different machine learning models, including SVR, BPNN, and XGBoost, to predict process parameters for WAAM. Furthermore, the SVR model was optimized by the Genetic Algorithm (GA) and Particle Swarm Optimization (PSO) algorithms. A 3D laser scanner was employed to obtain the weld bead's point cloud, and the weld bead size was extracted using the point cloud processing algorithm as the training data. The K-fold cross-validation strategy was applied to train and validate machine learning models. The comparison results showed that PSO–SVR predicted process parameters with the highest precision, with the RMSE,  $R^2$ , and MAE being 1.1670, 0.9879, and 0.8310, respectively. Based on the process parameters produced by PSO–SVR, an optimal process parameter combination was chosen by taking into comprehensive consideration the impacts of power consumption and efficiency. The effectiveness of the process parameter optimization method was proved through three groups of validation experiments, with the energy consumption of the first two groups decreasing by 10.68% and 11.47%, respectively.

**Keywords:** WAAM; process parameters; machine learning; point cloud; SVR



**Citation:** Zhang, H.; Bai, X.; Dong, H.; Zhang, H. Modelling and Prediction of Process Parameters with Low Energy Consumption in Wire Arc Additive Manufacturing Based on Machine Learning. *Metals* **2024**, *14*, 567. <https://doi.org/10.3390/met14050567>

Academic Editors: Petru Berce and Guido Di Bella

Received: 18 March 2024

Revised: 30 April 2024

Accepted: 9 May 2024

Published: 11 May 2024



**Copyright:** © 2024 by the authors. Licensee MDPI, Basel, Switzerland. This article is an open access article distributed under the terms and conditions of the Creative Commons Attribution (CC BY) license (<https://creativecommons.org/licenses/by/4.0/>).

## 1. Introduction

Additive manufacturing (AM) technology has gained significant attention in recent years owing to its notable advantages, including a short lead time, reduced material waste, and the capacity to produce intricate structures. Metal additive manufacturing technology can be categorized into laser additive manufacturing (LAM), electron beam additive manufacturing (EBAM), and WAAM based on the heat sources used. Compared with LAM and EBAM, WAAM can manufacture large, complex parts at higher deposition rates and lower costs [1–3].

WAAM employs an arc as a heat source to systematically construct three-dimensional components by depositing metal material layer by layer. The entire component is generally comprised of numerous weld beads. The weld bead morphology of each layer and each pass affects the subsequent deposition and the final shape and quality of the component. In general, the weld bead morphology of each layer is mainly determined by process parameters [4]. Dinovitzer et al. [5] used the Taguchi method and analysis of variance (ANOVA) to determine the effects of welding speed (WS), wire feed speed (WFS), welding

current, and argon flow rate on weld bead shape and size, and they discovered that WFS is the most significant factor. The quality of the weld bead is mainly determined by process parameters, including the welding current, welding voltage, and welding time, while the welding time is mainly related to the welding speed [6]. If the process parameters are not appropriately chosen, excessive heat input can result in deformation, high residual stresses [7], poor surface quality, and splatter phenomena [8]. Karlina et al. [9] emphasized the potential for optimizing process parameters to improve material characteristics. Thus, choosing the appropriate process parameter based on the deposition trajectory yielded by the slicing process is a critical step in the WAAM process.

Many researchers have been devoted to quantifying the association between process parameters and the response variables that characterize the morphology of the weld bead and optimizing process parameters using different mathematical methodologies, such as multiple regression analysis (MRA), finite element modelling (FEM), and machine learning. Sarathchandra et al. [10] evaluated the effects of the WS, welding current, and standoff distance on weld bead characteristics by response surface method in conjunction with ANOVA; they used MRA to establish a model between process parameters and weld bead quality. Le et al. [11] used Grey-Relational Analysis (GRA) and Techniques for Order-Preferences by Similarity-to Ideal Solution (TOPSIS) methods to determine the optimal process parameters. FEM-based modelling can investigate how process parameters affect the dimensional accuracy of the component and optimize process parameters [12,13]. Hanif et al. [14] employed FEM to study the temperature and thermal stress field in the TIG welding process and applied the GRA method to obtain the optimal weld bead geometry by comprehensively considering various factors such as welding current, shielding gas flow rate, and standoff distance on the weld bead.

Machine learning does not require any physics-based equations and only needs to use past experimental data to establish the relationship between input variables and output targets, which can quickly predict output targets. Sharma et al. [15] used three machine-learning algorithms to investigate the influence of WS, welding current, and the number of layers on weld bead morphology. Among them, random forest had the highest prediction accuracy for bead height and width, with 94% and 99% accuracy rates, respectively. Barrionuevo et al. [16] compared the performance of GPR, XGBR, and MLP algorithms in predicting melting efficiency by inputting the wire diameter, nominal power, WFS, and WS variables, finding that GPR had the highest prediction accuracy with an  $R^2$  of 0.9190. Yaseer et al. [17] used random forest and multilayer perceptron algorithms to predict the layer surface roughness in WAAM. Both algorithms could effectively model and predict layer roughness for the same data sets. Still, the random forest was superior to the multilayer perceptron algorithm in terms of accuracy and computational efficiency. Xia et al. [18] compared the performance of different machine learning algorithms in predicting the surface roughness of weld beads. The results showed that GA-ANFIS had the optimal prediction performance, with RMSE,  $R^2$ , MAE, and MAPE values of 0.0694, 0.93516, 0.0574, and 14.15%, respectively. Wang et al. [19] established an artificial neural network (ANN) with interlayer temperature, WFS, and WS as input variables to predict the bead width, height, and contact angle in cold metal transfer welding. The average error rate of the model was less than 5.1%. Lee [20] used the Gaussian process regression method to model the process parameters, which improved the productivity of WAAM and the shape and quality of the deposits. Yadav et al. [21] used MRA, FEM, and Back Propagation Neural Network (BPNN) to establish models with WFS, WS, welding voltage, and contact tip-to-substrate distance as input variables. The response surface method guided the experimental design and generates three geometric response variables. The results showed that BPNN had higher accuracy than the MAR and FEM methods. Evidently, the data-driven machine learning model predicted the results much closer to the experimental values than the physics-driven modelling method.

From the above literature review, it can be seen that the study of weld bead geometry has generated a great deal of interest in the WAAM field. However, only some researchers

have undertaken the inverse forecast of process parameters from the desired weld bead geometry. In the past, the operator had to choose the proper process parameter settings based on their experience and repeated tests. If the desired weld bead geometry can directly predict the process parameters in advance, not only can the energy consumption of the welder be reduced, but the weld bead quality can also be improved [22,23]. Venkata et al. [24] developed a method with ANN, FEM, and Taguchi-based graph theory to optimize the process parameters for ensuring dimensional accuracy in AM. Karmuhilan et al. [25] established an ANN with bead height and width as inputs and welding voltage, WFS, and WS as outputs. However, the number of response variables exceeds the number of input variables, which can easily lead to unstable prediction results, and the bead width and height are not enough to represent the geometric properties of the entire weld bead. This method of predicting process parameters by reverse modelling is ambiguous because different process parameters may result in the same weld bead geometry [26].

In order to address the issue of ambiguity in predicting process parameters through reverse modelling, this paper employed different machine learning algorithms to predict process parameters for WAAM and determined the optimal process parameters. Initially, a comparative analysis was conducted to evaluate the performance of different machine learning models in predicting process parameters. Then, the model with the highest level of prediction accuracy was utilized to optimize the process parameter. Considering the influence of power consumption and efficiency, the optimal process parameters were selected from the predicted values generated by the optimal machine learning model. Several groups of experiments were conducted utilizing the predicted process parameters to validate the accuracy of the predicted results and the effectiveness of the optimal parameters. This method avoids trial-and-error experiments, greatly shortens the time and cost expenditure, and has a certain guiding significance for selecting process parameters.

## 2. Methodology

### 2.1. Experimental Setup

The experiments were conducted on a WAAM system, as illustrated in Figure 1. It consists of a six-axis welding robot (ABB IRB1600, ABB, Zurich, Switzerland), a controller cabinet (ABB IRC5, ABB, Zurich, Switzerland), a MIG welder (SAF-FRODIGIPULS III 420, SHAF Electric, Shanghai, China), a 3D laser scanner (SR7400, SSZN, Shenzhen, China), and a control computer. The specifications for the 3D laser scanner are detailed in Table 1. The depositions were carried out on Q235 substrates with a thickness of 10 mm. Low-carbon steel materials are commonly used in WAAM due to their affordability and consistent mechanical properties. For this reason, the steel CHW-50C6 (Hantai Welding Technology, Changsha, China) with a diameter of 1.2 mm was selected as the filling material, and Q235 steel was used as the substrate. The main components of the welding wire and substrate are shown in Table 2. The shielding gas was a mixture of 20% CO<sub>2</sub> and 80% Ar with a flow rate of 18 L/min. The elongation of the welding wire was 12–15 mm. The welding voltage was set to be 22 V, while the welding current changed with the preset WFS.

**Table 1.** 3D laser scanner parameters.

Model	Scan Height	Scan X Length	Z-Axis Accuracy	X-Axis Accuracy	Single Line Points
SR7400	200 mm	240 mm	5 µm	90 µm	3200

**Table 2.** Composition of the used welding wire and substrate (wt. %).

Material	Composition (wt. %)					
	C	Mn	Si	S	P	Cu
CHW-50C6	0.08	1.52	0.92	0.015	0.020	0.20
Q235	≤0.17	≤1.4	≤0.35	≤0.035	≤0.035	-

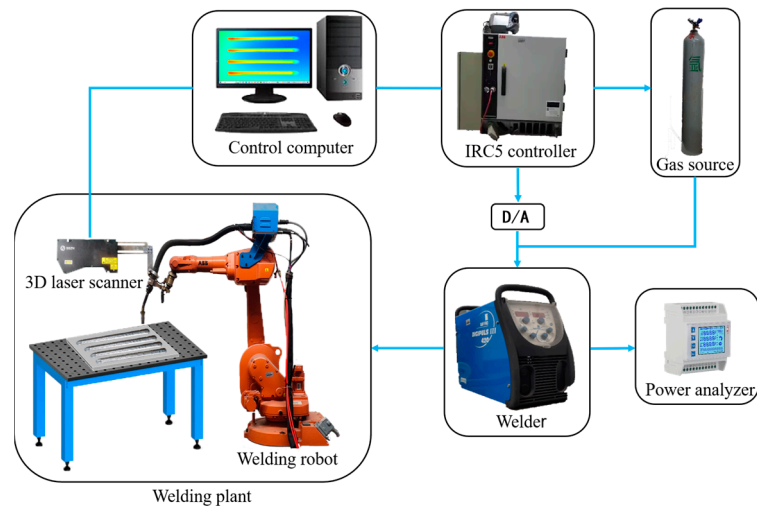


Figure 1. Schematic diagram of the experimental setup.

2.2. Experiment Design

Suitable process parameters ensure the geometric accuracy and performance of the weld. As shown in Figure 2, when the WFS/WS ratio is high, excessive metal materials are filled into the weld in a short period of time, making the molten pool larger and more susceptible to collapse. When the WFS/WS ratio is low, the amount of metal materials filled per unit time is insufficient, resulting in a spheroidization effect that makes the weld bead discontinuous, and a relatively high welding speed may result in a humped weld bead [27]. Only when the WFS/WS is in the proper range can the normal morphology of the weld bead be obtained. The main factor controlling the morphology of the weld bead is WFS/WS [28]. Hence, all possible combinations of 14 different WFS and 6 different WS were used in the experiments, as shown in Table 3. In other words, 84 weld beads were obtained by single-layer single-pass depositions if the process parameter combinations were reasonable. These weld beads were scanned to provide data sets for machine learning and subsequent process parameter optimization.

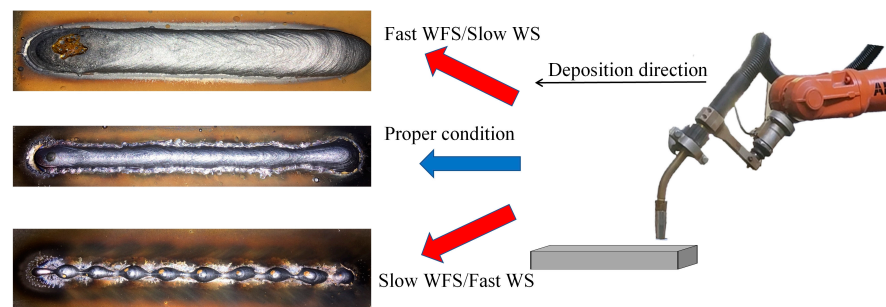


Figure 2. The effect of different WFS/WS on the weld morphology.

Table 3. Experiment design.

Parameters	Value
WFS (m/min)	3, 4, 5, 6, 7, 8
WS (mm/s)	3, 4, 5, 6, 7, 8, 9, 10, 11, 12, 13, 14, 15, 16

2.3. Data Sets Collection for Machine Learning Models

To provide data sets for predicting WFS/WS, the 3D laser scanner was used to extract the cross-section profiles of the weld bead, and then the cross-section profiles were modeled based on the mathematical function curve fitting method, which can obtain the dimensions

of the weld bead. Bead width (BW) and bead height (BH) are the geometrical variables used most frequently. However, measuring the BW and BH alone is insufficient to fully characterize its morphological properties. It is necessary to introduce bead cross-section area (BCSA) as the third geometric response variable. As a result, all machine learning models used the BH, BW, and BCSA data as their input set and the corresponding process parameter WFS/WS value as their output set. Additionally, K-fold cross-validation is used to reduce the overfitting of all machine learning models.

A total of 84 welds were deposited in accordance with the experimental design. Figure 3 shows the process of acquiring data sets for machine learning. After each deposition, the point cloud of the weld bead was obtained with the 3D laser scanner. Then, point cloud processing and curve fitting were used to obtain the cross-section profiles and the values of BH, BW, and BCSA. However, certain parameter combinations resulted in unsuccessful deposition with defects such as humps and pits. Those inapplicable combinations were ruled out, and only 64 weld beads were scanned to provide data sets. The detailed procedure for extracting the cross-section profiles and curve fitting will be discussed below.

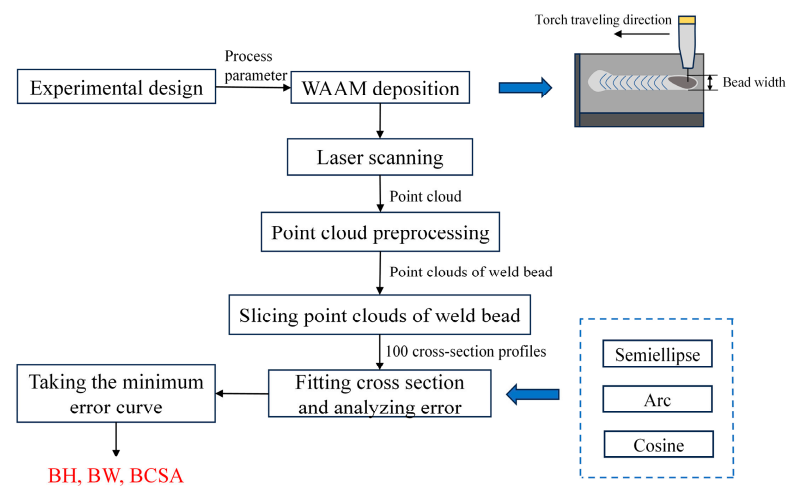


**Figure 3.** Schematic diagram to obtain machine learning data sets.

### 2.3.1. Extracting the Cross-Section Profiles of Weld Bead

As shown in Figure 4, the 3D laser scanner emitted laser stripes oriented perpendicularly to the deposition direction, and it employed the triangulation principle to obtain the coordinate information of the surface points, enabling the reconstruction of the three-dimensional morphology by the point cloud. The obtained point cloud data were processed using functions in the open-source Point Cloud Library (PCL) to extract the cross-section profiles of the weld bead. Firstly, the pass-through filter was used to segment the part of the weld to be detected. Secondly, the RANSAC algorithm was used to segment the weld bead from the substrate. Thirdly, sparse points near the weld bead were removed by applying the statistical filter to get a clean point cloud of the weld bead. Finally, 100 cross-section profiles were obtained by slicing the weld bead at 100 locations along the length direction. Generally, if the welding parameter stays constant, the cross-section profiles at different locations are similar. However, the slicing location should not be in the start and end areas of the weld bead because the ignition and quenching of the arc lead to unstable weld bead morphology. Even if not in the start and end areas, the profiles are still likely to vary slightly due to a variety of factors. Obtaining 100 cross-section profiles can significantly decrease accidental errors.

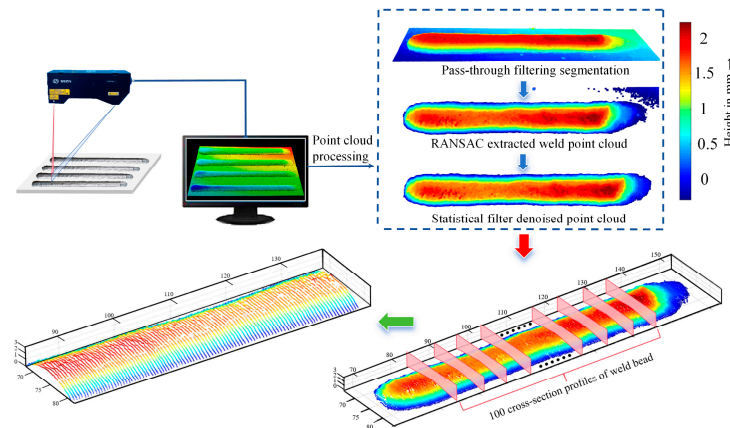


Figure 4. Schematic diagram to extract the cross-section profiles of weld bead.

### 2.3.2. Curve Fitting of Weld Bead Profiles

The cross-section profiles are generally arc-like curves. In many previous studies, the profiles were modeled using mathematical functions or geometrical parameters [29–31]. In this paper, the cross-section profiles of weld beads were modeled based on the methods of semi-ellipse, arc, and cosine function curve fitting, as shown in Table 4. Based on the acquired cross-section profiles, the process of curve fitting was carried out using three different mathematical models. Figure 5a shows that the semi-ellipse model accurately matched the actual profile on both sides but exhibited a downward tilt at the top, and the cosine model overshoot the actual profile at the top, while the arc model best matched the actual profile at both the sides and the top.

Table 4. Mathematical model of weld bead profile.

Profile Model	Functional Model	Bead Cross-Section Area (BCSA)
Cosine	$y = \text{acos}(bx)$	$\int_{-\frac{w}{2}}^{\frac{w}{2}} \text{acos}(bx) dx$
Arc	$y = \sqrt{b^2 - x^2} - a$	$\int_{-\frac{w}{2}}^{\frac{w}{2}} (\sqrt{b^2 - x^2} - a) dx$
Semi-ellipse	$y = \sqrt{b^2 - \frac{b^2x^2}{a^2}}$	$\int_{-\frac{w}{2}}^{\frac{w}{2}} \sqrt{b^2 - \frac{b^2x^2}{a^2}} dx$

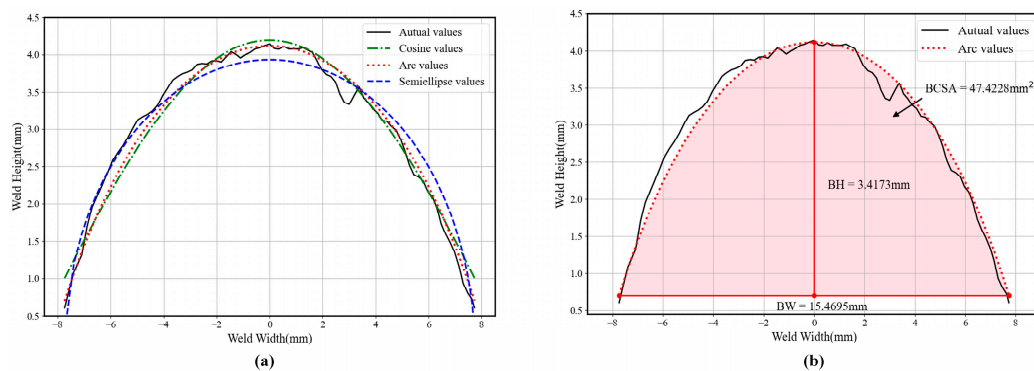


Figure 5. Weld bead modeling process. (a) One of the cross-section profiles and its fitted curves using three different functions; (b) calculating BH, BW, and BCSA after curve fitting of the arc function.

As mentioned in Section 2.3.1, 100 cross-sectional profiles with a length of 200 mm were collected and used for curve fitting to avoid accidental errors. Figure 6 shows the Root Mean Square Errors (RMSE) of the fitting curves for each profile. The arc model had the RMSE closest to 0, indicating the highest accuracy in the fitting. The semi-ellipse model showed the most significant error, particularly at the 22nd profile, where the RMSE exceeded 0.7. The cosine model’s error was between the arc and semi-elliptical models.

Thus, the arc function model was chosen as the final curve fitting model to determine the BH, BW, and BCSA, as shown in Figure 5b. Since 100 cross-section profiles were extracted for each weld bead, 100 groups of values for BH, BW, and BCSA could be obtained. The average values of them were used for data sets. As mentioned above, only 64 weld beads were scanned, and the collected whole data sets are shown in Table 5. When the WS value remained constant, the BH, BW, and BCSA increased as the WFS increased. Similarly, when the WFS value remained unchanged, the BH, BW, and BCSA decreased with the increase in WS, consistent with the experimental findings reported in [6,32,33].

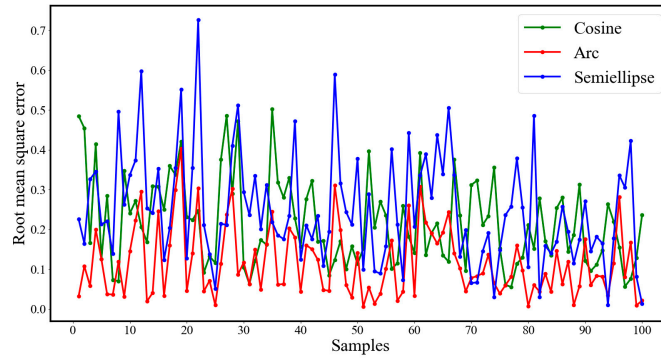


Figure 6. Root Mean Square Error of different mathematical functions.

Table 5. Data sets from experiments for each design.

No.	WFS (m/min)	WS (mm/s)	WFS/WS	BW (mm)	BH (mm)	BCSA (mm <sup>2</sup> )	No.	WFS (m/min)	WS (mm/s)	WFS/WS	BW (mm)	BH (mm)	BCSA (mm <sup>2</sup> )
1	3	3	16.67	7.46	2.63	14.33	33	6	8	12.50	5.82	2.45	10.76
2	4	3	22.22	9.33	2.76	18.35	34	7	8	14.58	6.54	2.78	13.71
3	5	3	27.78	10.08	3.26	23.64	35	8	8	16.67	6.89	2.95	15.36
4	6	3	33.33	11.08	3.43	27.18	36	4	9	7.41	4.04	1.91	5.99
5	7	3	38.89	12.49	3.81	34.01	37	5	9	9.26	4.65	2.21	7.96
6	8	3	44.44	13.56	3.67	35.09	38	6	9	11.11	4.85	2.44	9.30
7	3	4	12.50	6.07	2.42	10.92	39	7	9	12.96	6.09	2.65	12.23
8	4	4	16.67	8.34	2.63	15.76	40	8	9	14.81	6.38	2.81	13.63
9	5	4	20.83	8.84	2.86	18.16	41	4	10	6.67	3.77	1.94	5.77
10	6	4	25.00	9.38	3.13	21.24	42	5	10	8.33	4.68	2.12	7.59
11	7	4	29.17	10.87	3.57	27.93	43	6	10	10.00	4.73	2.19	7.96
12	8	4	33.33	11.40	3.62	29.62	44	7	10	11.67	5.80	2.59	11.46
13	3	5	10.00	4.87	2.30	8.68	45	8	10	13.33	5.98	2.70	12.38
14	4	5	13.33	6.37	2.44	11.49	46	4	11	6.06	3.65	1.93	5.60
15	5	5	16.67	7.45	2.86	15.78	47	8	11	12.12	5.55	2.76	11.99
16	6	5	20.00	7.90	2.77	15.94	48	4	12	5.56	3.34	1.87	5.06
17	7	5	23.33	9.22	3.25	21.87	49	5	12	6.94	3.78	1.98	5.94
18	8	5	26.67	10.09	3.35	24.41	50	6	12	8.33	4.00	1.99	6.25
19	3	6	8.33	4.24	2.17	7.27	51	7	12	9.72	4.95	2.15	8.06
20	4	6	11.11	5.24	2.14	8.38	52	8	12	11.11	5.21	2.49	10.09
21	5	6	13.89	6.48	2.72	13.24	53	5	13	6.41	3.66	1.93	5.63
22	6	6	16.67	7.10	2.75	14.47	54	6	13	7.69	5.42	2.04	8.13
23	7	6	19.44	7.93	3.06	17.99	55	7	13	8.97	4.54	2.14	7.50
24	8	6	22.22	8.97	3.22	21.11	56	8	13	10.26	5.11	2.38	9.37
25	3	7	7.14	3.95	2.05	6.40	57	5	14	5.95	3.37	1.93	5.32
26	4	7	9.52	4.87	2.21	8.26	58	6	14	7.14	4.68	1.89	6.59
27	5	7	11.90	5.69	2.48	10.74	59	7	14	8.33	4.27	2.05	6.80
28	6	7	14.29	6.31	2.57	12.12	60	8	14	9.52	4.76	2.34	8.69
29	7	7	16.67	7.22	2.95	15.92	61	7	15	7.78	4.25	2.07	6.87
30	3	8	6.25	3.57	1.92	5.50	62	8	15	8.89	4.71	2.33	8.60
31	4	8	8.33	4.50	2.10	7.27	63	7	16	7.29	3.86	1.97	6.01
32	5	8	10.42	5.37	2.34	9.52	64	8	16	8.33	4.38	2.25	10.76

### 2.4. Process Parameters Optimization Procedure

The procedure for process parameter optimization is illustrated in Figure 7. Three steps are included as follows:

- (1) Prediction of WFS/WS: Firstly, the BH and BW were set up to create the desired surface morphology, and the BCSA value was then calculated according to the arc mathematical function. Subsequently, the trained machine learning model was used to predict WFS/WS. The primary reason for choosing WFS/WS was to ensure the deposition quality. As discussed in Section 2.2, the morphology and success of the deposition were highly related to WFS/WS.
- (2) Calculation of candidate process parameters: Referring to the welding-feasible region diagram obtained from the previous experiment (Figure 8), multiple sets of process parameter combinations were generated by cyclic iteration and taken as candidate process parameters. Figure 8 demonstrates that even when the WFS/WS value is identical, the formation quality of the weld bead will have significant variations if the WFS or WS value is not chosen correctly. Hence, it was crucial to compute the WFS and WS values based on the summarized range of the welding-feasible area.
- (3) Choosing optimal process parameters among candidates: A machine learning model was established with process parameters as input to forward predict the BW and BH. The difference between the predicted and preset values was analyzed. If the error exceeded 5%, the corresponding combination would be removed. Finally, the optimal parameter combination was selected by maximizing the effective deposition volume per power (EDVP).

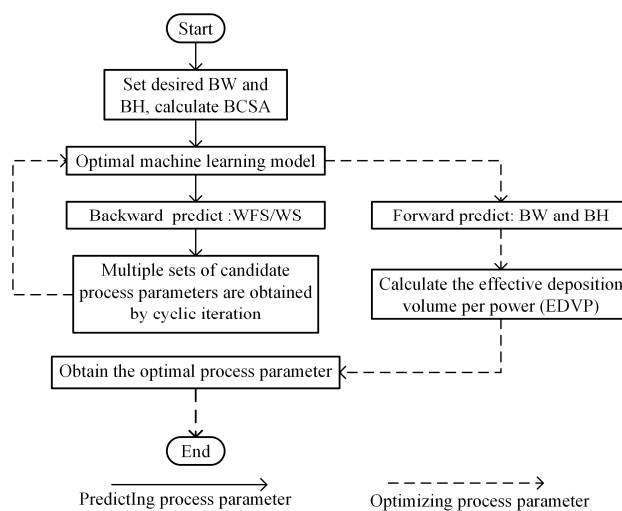


Figure 7. Flow chart of process parameter optimization.

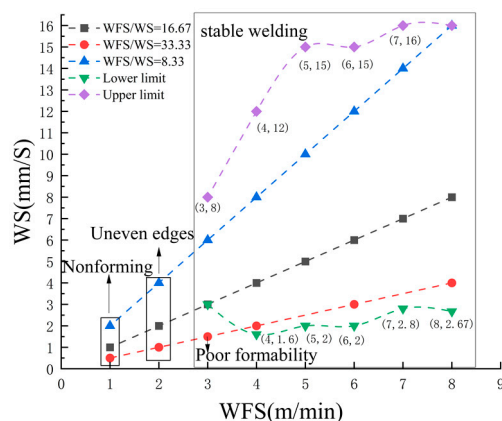


Figure 8. Diagram of a welding-feasible region.

It is worth mentioning that multiple ML algorithms were used for process parameter planning. The performances of those algorithms are compared, as presented in Section 4.1. The optimal algorithm was then chosen to perform the process parameter planning for the experiments, as shown in Section 4.3.

EDVP is an index regarding the influence of power consumption and efficiency. The value of EDVP can be calculated based on the following Equations (1)–(5).

$$V_{\text{effective}} = S \times L = BCSA \times L \quad (1)$$

where  $V_{\text{effective}}$ ,  $S$ , and  $L$  represent the effective deposition volume of the deposited sample, the effective area, and the sample effective length, respectively. The effective area is  $BSCA$ , which the arc mathematical function calculates.

$$V_{\text{total}} = WFS \times T \times \pi \times r^2 = WFS \times \frac{L}{WS} \times \pi \times r^2 \quad (2)$$

where  $V_{\text{total}}$ ,  $WFS$ , and  $T$  represent the total deposited volume, the wire feeding speed, and the duration of each welding cycle, determined by the total length and welding speed. And  $r$  indicates the wire radius, which is 0.6 mm in the experiments. The formula for computing the effective deposition rate ( $EDR$ ) is as follows:

$$EDR(\%) = \frac{V_{\text{effective}}}{V_{\text{total}}} \times 100\% \quad (3)$$

The calculation of the effective deposition rate per power ( $EDRP$ ) is performed using the following formula:

$$EDRP(\%/W) = EDR/P \quad (4)$$

where  $P$  represents the power of the welding supply. The formula for computing the effective deposition volume per power ( $EDVP$ ) is as follows:

$$EDVP(\text{mm}^3/W) = EDRP \times V_{\text{effective}} \quad (5)$$

### 3. Machine Learning Algorithms

#### 3.1. Support Vector Regression

Support vector regression (SVR) is a powerful machine learning algorithm widely used in regression analysis. Its principle is to use the kernel function to map input data to high-dimensional space to solve the optimal hyperplane and transform the nonlinear relationship between input and output variables into a linear relationship for prediction [34]. The expression of the SVR model is as follows:

$$f(x) = \sum_{i=1}^m (\alpha_i - \alpha_i^*) K(x_i, x_j) + b \quad (6)$$

where  $\alpha_i$  and  $\alpha_i^*$  are Lagrange multipliers;  $b$  denotes intercept;  $K(x_i, x_j)$  is the kernel function. In order to improve the nonlinear processing ability of the SVR model, the Gaussian radial basis function (RBF) is usually used as the kernel function. The RBF function is as follows:

$$K(x_i, x_j) = \exp\left(-\frac{\|x_i - x_j\|^2}{g^2}\right) \quad (7)$$

In the SVR model, the penalty factor  $C$  and RBF function parameter  $g$  directly determine the prediction performance of the model. The generalization of the model is influenced by the parameter  $C$ , while the training speed of the model is influenced by the parameter  $g$ . Therefore, it is important to reasonably select appropriate values for these two parameters. This study employs search ranges of (0.1, 200) for the  $C$  and (0.001, 1) for the  $g$ .

### 3.2. XGBoost

XGBoost reduces the error of the previous prediction by continuously generating new regression trees, gradually narrows the gap between the true value and the predicted value, and ultimately improves the model's prediction accuracy [35]. The prediction function of XGBoost is as follows:

$$\hat{y}_i = \sum_{k=1}^K f_k(x_i), f_k \in \Gamma \quad (8)$$

where  $\hat{y}_i$  the predicted output value of the  $i$ th sample;  $K$  is the total number of regression trees;  $f_k$  is the predicted value of the  $k$ th model in the  $i$ th sample;  $\Gamma$  is the space of the regression tree. The objective function is as follows:

$$Obj = \sum_{i=1}^n l(y_i, \hat{y}_i) + \sum_{k=1}^K \Omega(f_k) \quad (9)$$

where  $Obj$  is the objective function;  $\sum_{i=1}^n l(y_i, \hat{y}_i)$  is the loss function, indicating the fitting degree of the model;  $\Omega(f_k)$  is a penalty function to reduce the risk of overfitting. The number of decision trees, the maximum depth of the tree, and the learning rate are the three key hyperparameters of XGBoost. In this paper, the search range of the number of decision trees, the maximum depth of the tree, and the learning rate are [50, 100, 200, 400, 500], [3, 4, 5, 6, 7, 8, 9, 10], and [0.01, 0.05, 0.1, 0.15, 0.2], respectively.

### 3.3. Back Propagation Neural Network

BPNN is a multi-layer feedforward neural network with error back-propagation. Through the back-propagation of errors, the weights and thresholds of the network are constantly adjusted to minimize the mean square error of the network [36]. As shown in Figure 9, the structure of the BP neural network model consists of an input layer, a hidden layer, and an output layer. In this experiment, the input layer nodes are BW, BH, and BCSA, respectively, and the output layer nodes are WFS and WS. When there is information input, the input information is sent to the input node, and after the hidden layer is processed by the function, it is sent to the output node. When the neural network has no activation function, the final output result is linear, and nonlinear data prediction cannot be performed [37]. Thus, it is necessary to add activation functions to the neural network model. This paper used the sigmoid function, the tanh function, and the ReLU function as the activation functions of the hidden layer. The neuron nodes of the hidden layer were in the range of 10–40, and different optimization algorithm solvers (SGD, LBFGS, Adam) were used to find the optimal weight to minimize the loss function. The number of iterations was 500.

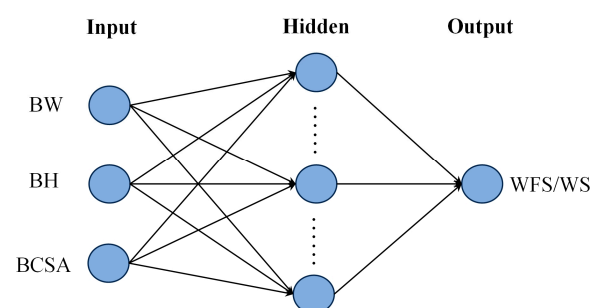


**Figure 9.** Back Propagation Neural Network architecture.

### 3.4. Machine Learning Tools

This paper mainly uses PyCharm software (Community Edition 2022.2.2) to write machine learning code based on Python. Python is an open-source programming language

widely used to develop machine learning algorithms. PyCharm software provides powerful code analysis tools to help developers improve development efficiency and code quality. The essential libraries, including NumPy, Pandas, Scikit-learn, XGBoost, and Matplotlib, were imported into PyCharm before the machine learning codes and data visualization were executed.

### 3.5. Evaluation of Machine Learning Algorithms

To better evaluate the established machine learning model, this paper employs metrics such as Mean Absolute Error (MAE), Root Mean Square Error (RMSE), and the Coefficient of Determination ( $R^2$ ) for evaluation and comparative analysis. The MAE is usually used to weigh the absolute error between the actual and predicted values of the model. The disadvantage of MAE is that it only considers the average of absolute errors and is not sensitive to outliers. The RMSE is used to weigh the deviation between predicted and actual values. The  $R^2$  evaluates the prediction accuracy of different models. Among them, the smaller the MAE and RMSE values, the closer the model predicted value is to the actual value, the closer the  $R^2$  value is to 1, and the better the model fitting performance. The expression of the three metrics is as follows:

$$MAE = \frac{1}{n} \sum_{i=1}^n |y_i - \hat{y}_i| \quad (10)$$

$$RMSE = \sqrt{\frac{1}{n} \sum_{i=1}^n (y_i - \bar{y}_i)^2} \quad (11)$$

$$R^2 = 1 - \frac{\sum_{i=1}^n (y_i - \hat{y}_i)^2}{\sum_{i=1}^n (y_i - \bar{y})^2} \quad (12)$$

where  $y_i$ ,  $\hat{y}_i$ ,  $\bar{y}$ , and  $n$  represent the actual value, the predicted value, the average of actual values, and the total of input data, respectively.

## 4. Results and Discussion

### 4.1. Comparing Different Machine Learning Models Prediction Results

Multiple algorithms, including SVR, XGBoost, and BPNN, were employed to predict the process parameters of WAAM. The K-fold cross-validation method was used to train and validate the model using the data sets obtained from the experiments. K-fold cross-validation is a resampling procedure employed to evaluate the precision of models when dealing with limited data sets [38]. This method randomly divides the original data sets into K discrete subsets. One of the subsets is designated as the validation data set, while the remaining K−1 subsets are dedicated to training. This process is repeated K times, and each subset takes turns as the validation set. In this study, the value of K was selected as 5, and 80% of the data sets were used for training, while the remaining 20% were reserved for model regression testing. The prediction results of different machine learning models were compared, and the model with the highest prediction accuracy was selected to plan process parameters.

The grid search is used to find the hyperparameters of the above machine learning, and the results are shown in Table 6. As shown in Figure 10, the predicted value of SVR was in good agreement with the actual value, while XGBoost had the lowest prediction accuracy. BPNN displayed signs of overfitting during the training process, resulting in unstable prediction outcomes. Although most points predicted by BPNN were consistent, the individual point deviation was relatively substantial, making the overall prediction accuracy not ideal. As shown in Table 7, the  $R^2$  value of the BPNN test set was 0.9170, while the  $R^2$  value of the training set was 0.9961. The  $R^2$  value of the test set was lower than the  $R^2$  value of the training set, and there was a potential overfitting phenomenon. The RMSE values of SVR, XGBoost, and BPNN were 1.8087, 2.0739, and 3.0545, respectively. The SVR achieved a higher prediction accuracy, but it still fell short of meeting the accuracy requirements for welding process parameter planning. Consequently, there was a

decision to optimize SVR through hyper-parameter tuning to enhance prediction accuracy and stability.

**Table 6.** Optimal hyper-parameters in different machine learning algorithms.

Machine Learning Model	Parameter	Value	Parameter	Value	Parameter	Value
SVR	kernel	RBF	C	100	Gamma	0.0001
XGBoost	max_depth	6	learning_rate	0.05	n_estimators	400
BPNN	activation	tanh	Hidden layer sizes	10	solver	lbfgs

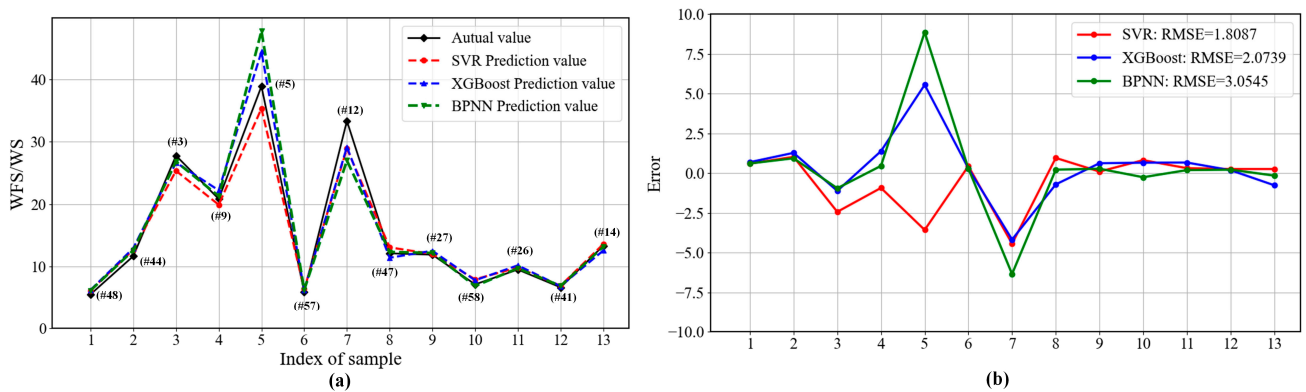


**Figure 10.** Predictions of different machine learning. (a) Comparison of the predicted and actual values of WFS/WS (# represents the corresponding serial number in Table 5); (b) error analysis of WFS/WS prediction.

**Table 7.** Performance comparison of training sets and test sets in different machine learning algorithms.

	Training			Testing		
	RMSE	MAE	R <sup>2</sup>	RMSE	MAE	R <sup>2</sup>
SVR	1.5165	0.8077	0.9663	1.8087	1.2413	0.9709
XGBoost	2.6030	1.2569	0.9196	2.0739	1.3916	0.9617
BPNN	0.6478	0.4667	0.9961	3.0545	1.5200	0.9170

#### 4.2. Comparing the Effect of GA and PSO on SVR

The traditional hyper-parameter tuning methods mainly use manual tuning, grid searching, and random searching [39]. For example, the above three machine learning models derive their hyperparameters through grid search. However, this method has corresponding defects, such as a long calculation time, an inability to deal with continuous parameters, ignoring the correlation between parameters, etc. Grid search is unsuitable for non-convex optimization problems and may also produce overfitting. Random search offers higher computational efficiency and broader coverage of the search space than grid search. However, it still exhibits instability with fewer data samples and cannot ensure a globally optimal solution exists. As a result, this study employs PSO and GA to optimize SVR parameters in the training scheme for complicated issues to improve the global search capabilities of the model and circumvent the local optimum, as shown in Figure 11.

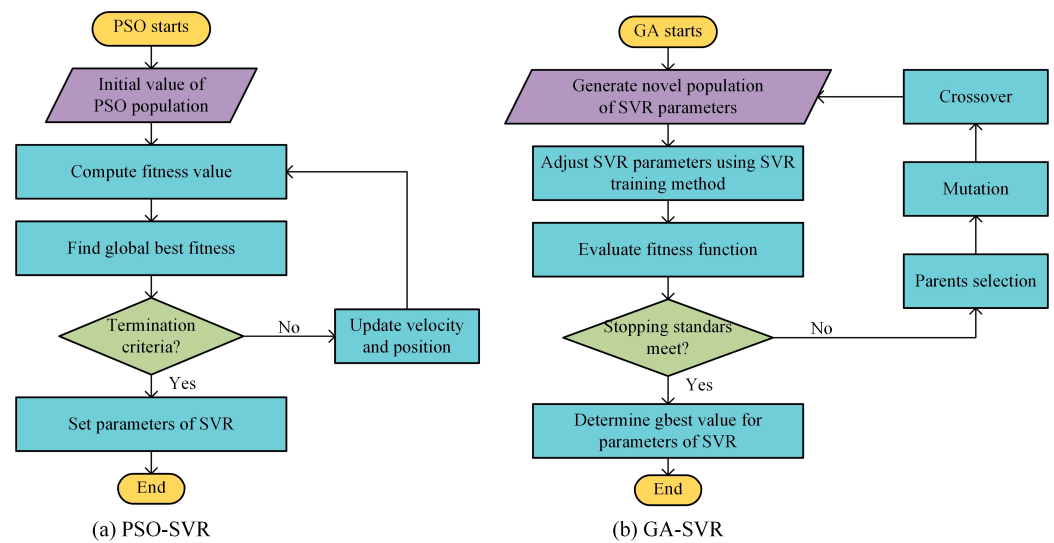


**Figure 11.** Scheme of GA-SVR and PSO-SVR algorithm. (a) PSO-SVR; (b) GA-SVR.

The primary parameters of the PSO algorithm include the number of particle swarms, the maximum number of iterations, the acceleration constants  $C1$  and  $C2$ , and the weight coefficient. The main parameters of the GA algorithm include population size, the maximum number of iterations, crossover rate, mutation rate, and DNA size. Population size significantly impacts the performance and effectiveness of GA and PSO. Therefore, this study observed the performance of PSO-SVR and GA-SVR under different population sizes using the trial-and-error method, as shown in Table 8.

**Table 8.** Performance of the model for various population sizes.

Population Size	PSO-SVR Result		GA-SVR Results	
	RMSE	$R^2$	RMSE	$R^2$
20	2.0522	0.9614	3.3094	0.9025
30	2.0830	0.9690	3.1986	0.9090
40	1.8269	0.9703	3.0348	0.9180
50	1.8464	0.9697	2.7042	0.9349
60	1.1670	0.9879	2.6308	0.9384
70	1.2653	0.9858	2.5409	0.9425
80	1.5696	0.9781	2.1823	0.9576
90	1.5841	0.9777	2.6461	0.9377

In the PSO-SVR algorithm, it can be observed that the increase in population size from 20 to 60 corresponded to the decrease in RMSE value. However, when the population increased from 60 to 90, the RMSE value increased. Therefore, PSO-SVR performed the best prediction when the population size was 60. In the GA-SVR algorithm, the RMSE gradually reduced as the population size rose from 20 to 80. When the population was 80, the RMSE value reached its lowest value. As a result, the ultimate population sizes for PSO and GA were determined to be 60 and 50, respectively. In addition, other parameters were also determined by the trial-and-error method, as shown in Table 9. The performance of PSO-SVR and GA-SVR is shown in Figures 12 and 13, respectively. Among them, PSO-SVR achieved the highest predictive accuracy, with RMSE values of 1.1670. The RMSE value of GA-SVR was 2.1823. Compared with the normal SVR in Figure 10, PSO-SVR can obtain better prediction performance. On the contrary, GA-SVR's prediction accuracy was lower than the normal SVR's, which did not play an optimization role.

**Table 9.** Model parameters of GA–SVR and PSO–SVR.

PSO		GA	
Number of particle swarm	60	Population size	80
Maximum number of iterations	220	Maximum number of iterations	700
Cognitive acceleration C1	1.5	Crossover rate	0.85
Social acceleration C2	3	Mutation rate	0.097
Initial inertia weight W1	0.85	DNA size	25

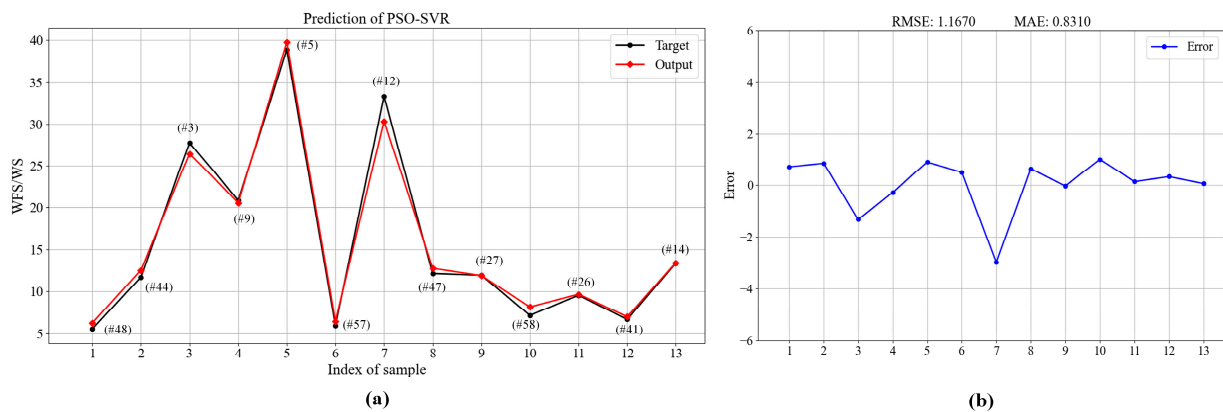


**Figure 12.** Prediction of PSO–SVR. (a) Comparison of the predicted and actual values of WFS/WS (# represents the corresponding serial number in Table 5); (b) error analysis of WFS/WS prediction.

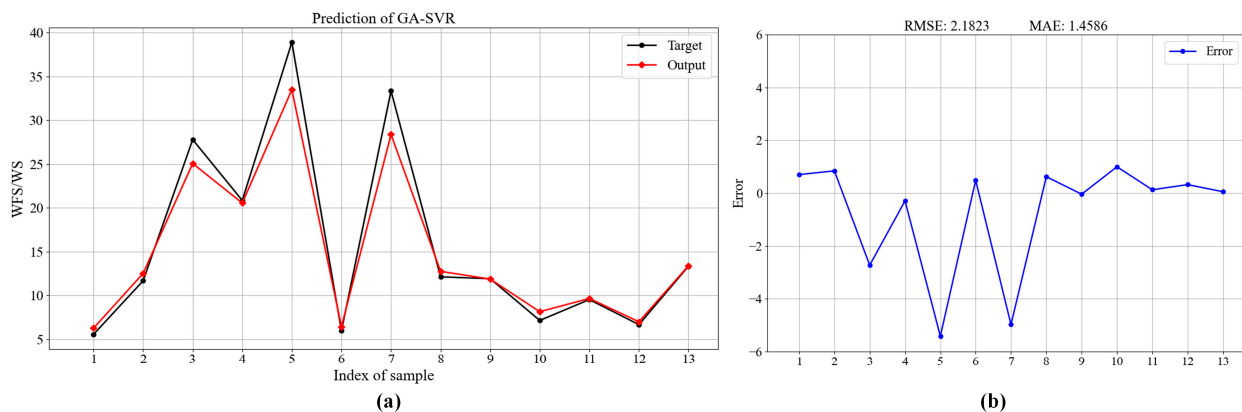


**Figure 13.** Prediction of GA–SVR. (a) Comparison of the predicted and actual values of WFS/WS; (b) error analysis of WFS/WS prediction.

In order to facilitate a more comprehensive comparison of the results, it was necessary to calculate the  $R^2$  of the prediction model using Equation (12). As shown in Figure 14, the correlation between the actual WFS/WS and the predicted WFS/WS values generated using different machine learning models is intuitively depicted. The distance between the surrounding scattered data points and the fitted line (representing the actual WFS/WS) shows the degree of correlation between the model-predicted value and the observed value. During the training and testing of the predictive models using K-fold cross-validation, the  $R^2$  values of SVR, XGBoost, BPNN, PSO–SVR, and GA–SVR were 0.9709, 0.9617, 0.9170, 0.9879, and 0.9576, respectively. The results show that the correlation coefficient  $R^2$  value of PSO–SVR was closer to 1 than that of GA–SVR, SVR, XGBoost, and BPNN. It can be inferred that among all the applied machine learning models, the PSO–SVR performed better in predicting the welding process parameters (WFS/WS) in WAAM. In addition, the PSO–SVR was also used to forward predict the bead height and width.

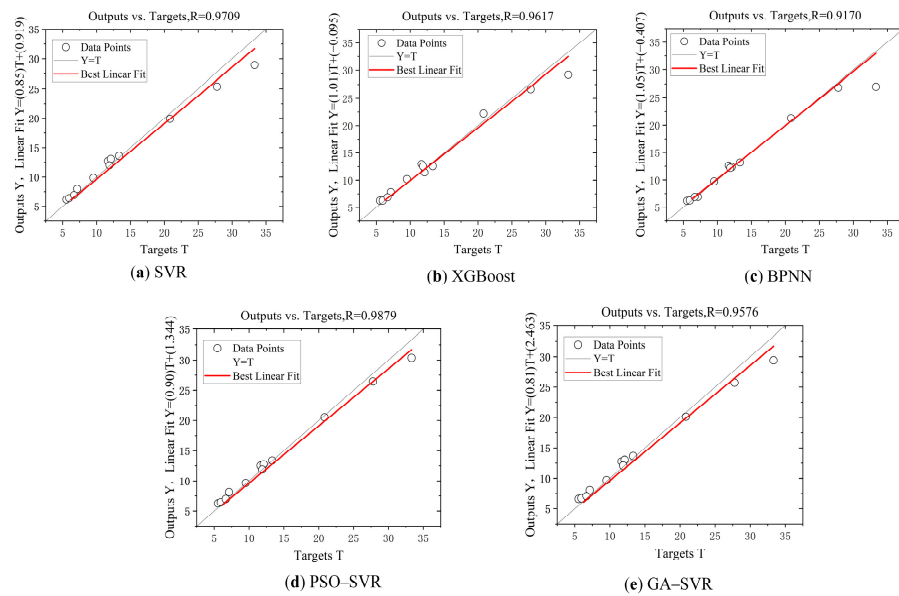


**Figure 14.** Regression plot for different models ‘predictions. (a) SVR; (b) XGBoost; (c) BPNN; (d) PSO-SVR; (e) GA-SVR.

### 4.3. Validation Experiment

To assess the efficacy of the process parameter optimization method, this study conducted three sets of verification experiments. The first group consisted of single-layer single-pass experiments, while the second group involved multi-layer single-pass curve experiments, and the third group is multi-layer multi-pass experiments. The process parameter optimization was performed based on the predicted results of the PSO-SVR algorithm, which demonstrated the highest prediction performance, as discussed in Section 4.2. In the experimental verification section, we used the power analyzer to measure the energy consumption of all candidate processes in the actual deposition process. The percentage of maximum energy savings can be calculated by comparing the energy consumption of the optimized process parameters with other parameters. The formula is as follows:

$$\eta = \frac{E_{\max} - E_o}{E_{\max}} \times 100\% \quad (13)$$

where  $E_o$  is the actual energy consumption of the optimized process parameters, and  $E_{\max}$  is the largest energy consumption value among other process parameters.

#### 4.3.1. Single-Layer Single-Pass Deposition

Single-layer single-pass experiments used a sample weld with bead dimensions of 11.4 mm in width, 3.6 mm in height, and 180 mm in length to verify the effectiveness of the process parameter optimization method. The BCSA can be determined as 29.43 mm<sup>2</sup> using the arc mathematical function. Firstly, the trained PSO-SVR machine learning model was utilized to input the BH (3.6 mm), BW (11.4 mm), and BCSA (29.43 mm<sup>2</sup>) to obtain a WFS/WS value of 33.008. Secondly, 12 sets of candidate process parameters can be determined by cyclic iteration based on the welding-feasible region diagram in Figure 8. Thirdly, these candidate process parameters were input to forward predict the bead width and height based on the PSO-SVR model and compare the error between the predicted size and the preset value. If the comprehensive error of the height and width of the weld bead exceeded 5%, the parameter was removed from the candidate process parameters. As shown in Figure 15c, the total error of the first set of process parameters was 7.03%, which did not meet the requirements of the error range. Lastly, considering the relationship between EDVP and welder energy consumption, the optimal process parameters were selected from the candidate process parameters by maximizing EDVP. The

calculation of EDVP can be determined by Equations (1)–(5). As shown in Table 10, it can be observed that the group labelled No. 7 exhibited the highest value for the EDVP, indicating that it represents the optimal combination of process parameters. Conversely, the group identified as No. 2 displayed the lowest value for the EDVP, indicating that it represents the worst combination of process parameters. Subsequently, experiments were conducted on individual candidate process parameters, and the welding energy consumption during the deposition process was measured with a power analyzer to verify the accuracy of the optimal process parameters.

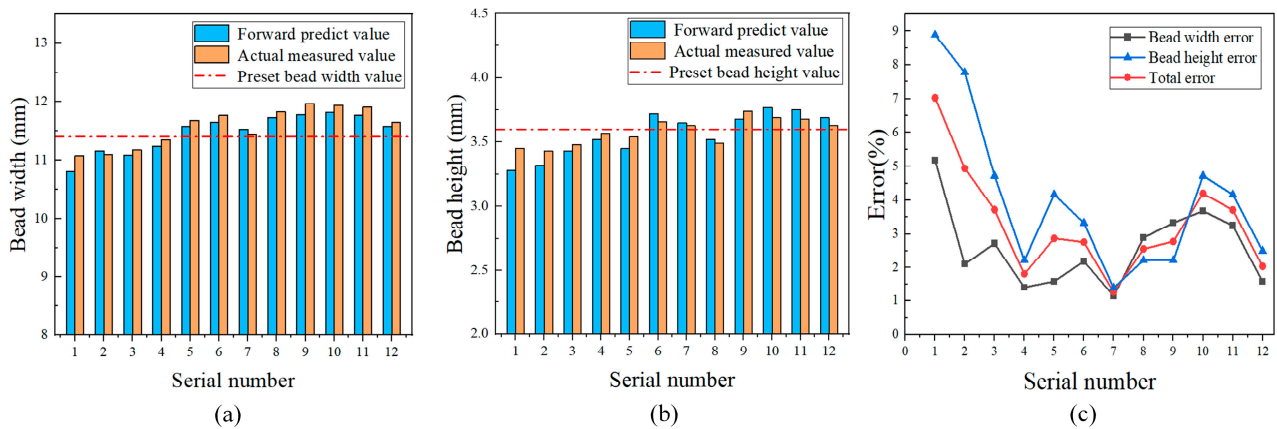


**Figure 15.** The comparison of preset the size of weld bead, forward predicted bead size, and actual measured size. (a) Comparison of weld bead width; (b) comparison of weld bead height; (c) error analysis between preset value and forward predictive value.

**Table 10.** Single-layer single-pass experimental design and results.

No.	WFS (m/min)	WS (mm/s)	BW (mm)	BH (mm)	BCSA (mm <sup>2</sup> )	EDRP (%W)	EDVP (mm <sup>3</sup> /W)	E (Wh)
1	3	1.5	10.81	3.28	-	-	-	-
2	3.5	1.75	11.16	3.32	26.17	0.005184	24.4178	76.2173
3	4	2	11.09	3.43	27.21	0.005237	25.6443	74.4883
4	4.5	2.25	11.24	3.52	28.34	0.005270	26.8870	72.2443
5	5	2.5	11.58	3.45	28.44	0.005120	26.2076	72.4333
6	5.5	2.75	11.65	3.72	31.13	0.005264	29.4933	70.9679
7	6	3	11.53	3.65	30.19	0.005564	30.2357	68.1638
8	6.5	3.25	11.73	3.52	29.42	0.004829	25.5683	75.4061
9	7	3.5	11.78	3.68	31.04	0.004950	27.6606	71.8503
10	7.5	3.75	11.82	3.77	32.00	0.004961	28.5747	71.3896
11	8	4	11.77	3.75	31.69	0.004654	26.5502	72.3520
12	8.5	4.25	11.58	3.69	30.68	0.004667	25.7723	73.1400

The results of the weld bead deposition utilizing the candidate process parameters are shown in Figure 16. It can be seen that the actual weld morphology and quality under different process parameter combinations were similar, aligning with the expected setting. As shown in Figure 15a,b, the actual measured bead width and height value fluctuated roughly around the preset value, and the predicted value was mostly close to the actual value. The power analyzer record indicates that the minimum energy consumption of the No. 7 group was 68.1638 Wh, while the maximum energy consumption of the No. 2 group was recorded at 76.2173 Wh. The process parameter combination of the minimum energy consumption index was consistent with the previously planned process parameter combination. Under the equivalent welding quality and morphology conditions, the optimized process parameters can save up to 10.68% of energy (Equation (13)).

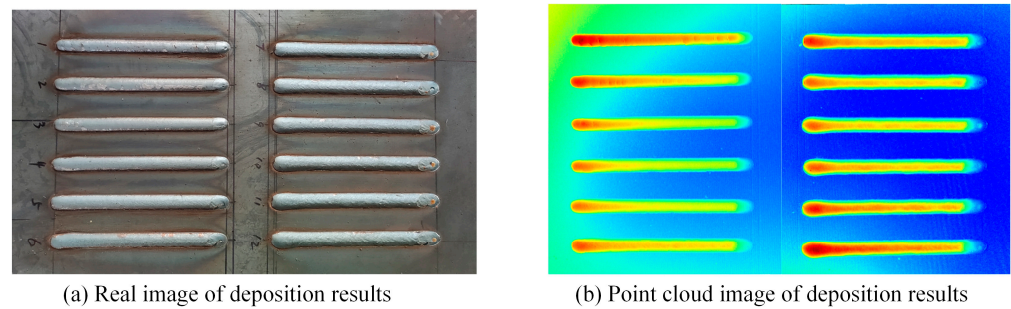


**Figure 16.** Single-layer single-pass deposition diagram (The serial number in subfigure (a) corresponds to Table 10).

#### 4.3.2. Multi-Layer Single-Pass Curve Deposition

Multi-layer single-pass curve deposition was conducted to assess the effectiveness of the process parameter planning method for complex-shaped components. Firstly, the preset width of the weld bead was 7 mm, the height of the weld bead was 3 mm, the length of the curve weld bead was 800 mm, and the number of bead layers was 10. The BCSA can be calculated to be 15.88 mm<sup>2</sup> by the arc mathematical function. The WFS/WS predicted by the trained PSO-SVR model was 16.42. Secondly, 10 sets of candidate process parameters can be obtained by cyclic iteration, as shown in Table 11. Thirdly, the optimal process parameters obtained by the process parameter optimization method were in the No. 4 group. Then, experimental validation was conducted, whereby distinct candidate process parameter combinations were utilized for each layer of multi-layer single-pass curve deposition. The outcomes of the deposition are shown in Figure 17. The measurement results of the power analyzer show that the lowest energy consumption of No. 4 was 145.73 Wh, which is consistent with the planned combination of process parameters. In this multi-layer single-pass verification experiment, the process parameter planning method can save up to 11.95% of energy by Equation (13), which once again verifies the effectiveness of the process parameter optimization method.

**Table 11.** Multi-layer single-pass experimental design and results.

No.	WFS (m/min)	WS (mm/s)	BW (mm)	BH (mm)	BCSA (mm <sup>2</sup> )	EDRP (%W)	EDVP (mm <sup>3</sup> /W)	E (Wh)
1	3	3	6.64	2.80	13.98	0.005952	66.5557	149.17
2	4	4	7.59	2.57	14.13	0.005833	65.9297	154.56
3	4.5	4.5	7.62	2.60	14.37	0.005871	67.4775	147.13
4	5	5	7.58	2.73	15.14	0.005674	68.7044	145.73
5	5.5	5.5	7.40	2.78	15.16	0.005383	65.2717	155.69
6	6	6	7.36	2.84	15.48	0.004871	60.3053	158.91
7	6.5	6.5	7.25	2.92	15.80	0.004399	55.6153	161.51
8	7	7	7.12	2.90	15.45	0.003946	48.7675	162.53
9	7.5	7.5	7.06	2.97	15.79	0.003848	48.6187	164.14
10	8	8	7.02	3.04	16.18	0.003635	47.0386	165.50

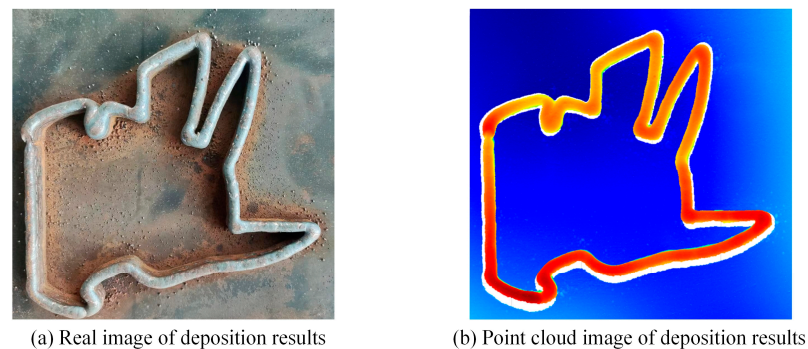


**Figure 17.** Multi-layer single pass curve deposition diagram.

#### 4.3.3. Multi-Layer Multi-Pass Deposition

To further verify the actual effect of the process parameter optimization method in this paper, multi-layer multi-pass verification experiments were carried out. Three  $100 \times 60 \times 8 \text{ mm}^3$  cuboid components were deposited in the multi-layer multi-pass experiment, and the process parameters #4, #7, and #12 in Table 10 from the single-layer single-pass experiment were respectively used for the experiment. The process parameters in #7 are the optimal combination of process parameters after optimization. The process parameters of the three groups of experiments were predicted by the same size of weld bead shape. It can be seen that the bead width and height of the actual deposited single bead were basically the same as the preset value in Section 4.3.1, and the bead height and width were 3.6 mm and 11.40 mm, respectively. According to the size of the single bead, to realize the formation of  $100 \times 60 \times 8 \text{ mm}^3$  cuboid components, each layer needed to deposit five welds, the overlap rate between adjacent welds was 60%, and the Z-shaped reciprocating deposition had three layers, as shown in Figure 18a. During the deposition process, the power analyzer was used to record the energy consumption and time of each group of experiments, and each layer was cooled for 3–5 min after the end of the deposition to avoid excessive heat accumulation. The 3D laser scanner can also be utilized to measure the geometric size of each layer of weld bead in the cooling period, as shown in Figure 18b. As shown in Figure 19, it can be found that the surface shape and quality of the weld bead after deposition of the process parameters of #7 were better than those of the other two sets of parameters. For example, the surface of the weld bead in Figure 19a was uneven, and even pores appeared, indicating that the selection of reasonable process parameters can even play a role in inhibiting defects. As shown in Table 12, the size of the deposited components of #7 process parameters was closest to the expected size, and the time and energy consumption of the process were significantly lower than those of the other two groups of experiments. In terms of energy consumption, #7 was 8.45% and 7.48% lower than #4 and #12, respectively. It was proved again that the process parameter optimization method in this paper can save energy consumption, reduce production costs, and achieve green manufacturing.

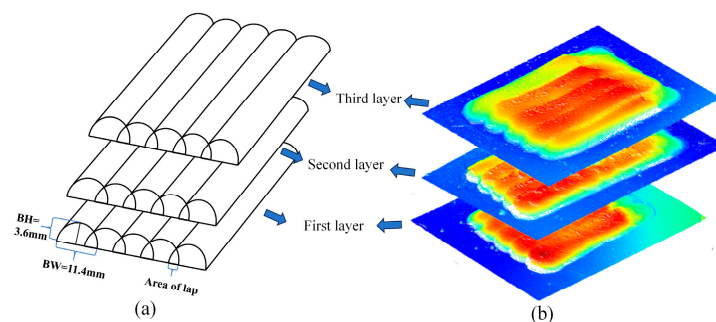


**Figure 18.** (a) Multi-layer multi-pass deposition schematic diagram; (b) the point cloud diagram of #7 process parameter deposition results measured by the 3D laser scanner.

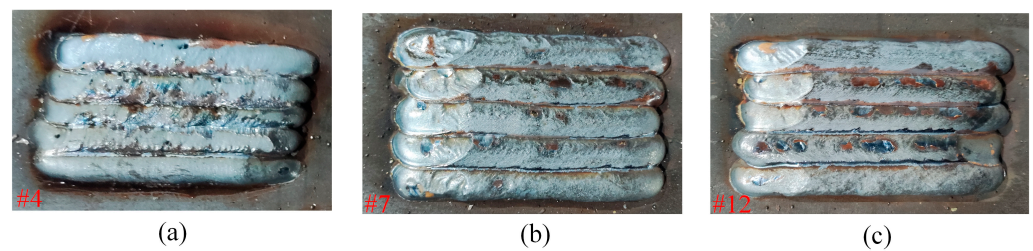


**Figure 19.** Multi-layer multi-pass deposition results. (a) #4 process parameter deposition results; (b) #7 process parameter deposition results; (c) #12 process parameter deposition results.

**Table 12.** Multi-layer multi-pass experimental results.

Group	WFS (m/min)	WS (mm/s)	Length (mm)	Width (mm)	Heigh (mm)	Processing Time (min)	E (Wh)
#4	4.50	2.25	96.96	58.83	8.54	10.53	549.38
#7	6.00	3.00	97.85	63.31	7.52	5.75	502.94
#12	8.50	4.25	100.24	61.37	8.16	5.00	543.62

## 5. Conclusions

This paper presents a method of process parameter optimization for WAAM based on machine learning. Different machine learning algorithms were utilized and compared in terms of performance. With machine learning models, the WFS/WS ratio was first predicted, and then the optimal process parameters were chosen by taking into account the impacts on power consumption and efficiency. The following conclusions can be drawn from this study:

- (1) Not only bead width (BW) and bead height (BH) but also Bead Cross-Section Area (BCSA) were used as geometric response variables in machine learning models. To calculate BCAS quickly, three mathematical functions were utilized to describe the profile of weld beads. Among them, the arc mathematical function was the closest to the actual cross-sectional profile, and the fitting accuracy was the highest, followed by the semi-elliptic and cosine functions.
- (2) K-fold cross-validation was used to assess the prediction performance of the machine learning models to maximize the use of training data. The results revealed that the SVR model had the highest prediction accuracy, with an RMSE of 1.8087 and an  $R^2$  of 0.9709. Conversely, XGBoost demonstrated the lowest accuracy. Notably, BPNN tends to overfit when working with small sample data sets, resulting in lower prediction accuracy for the test set than the training set.
- (3) To enhance the performance of the SVR, GA and PSO were applied to optimize the parameters of the SVR. The results showed that PSO-SVR has the highest prediction performance among the developed models, with an RMSE of 1.1670 and an  $R^2$  of 0.9879. Compared with SVR, the prediction accuracy is greatly improved.
- (4) The selection of the optimal process parameter considering the effective deposition volume per power can reduce the welding energy consumption to some extent. The optimized process parameters in the first single-layer single-pass experiment can save up to 10.68% energy. In the multi-layer single-bead validation experiment, the optimized parameters realized energy savings of up to 11.47%. The third set of verification experiments further verified the effectiveness of the process parameter optimization method.

In the future, more machine learning algorithms can be introduced and trained with larger amounts of data to improve the accuracy and robustness of predicting. By combining the slicing program with this parameter planning, a fully automatic WAAM system can be developed to achieve higher efficiency and lower energy consumption.

**Author Contributions:** Conceptualization, X.B. and H.Z. (Haiou Zhang); methodology, H.Z. (Haitao Zhang), X.B. and H.D.; software, H.Z. (Haitao Zhang) and H.D.; validation, H.Z. (Haitao Zhang); formal analysis, H.Z. (Haitao Zhang), and X.B.; investigation, H.Z. (Haitao Zhang); resources, H.Z. (Haiou Zhang) and X.B.; data curation, H.Z. (Haitao Zhang); writing—original draft preparation, H.Z. (Haitao Zhang); writing—review and editing, X.B.; visualization, H.Z. (Haitao Zhang) and X.B.; supervision, X.B.; project administration, H.Z. (Haitao Zhang) and X.B.; funding acquisition, X.B. All authors have read and agreed to the published version of the manuscript.

**Funding:** This work was supported by the Natural Science Foundation of Hunan Province (Grant No. 2023JJ30510), National Natural Science Foundation of China (Grant No. 51975270), key project of the Education Department of Hunan Province, China (Grant No. 21A0257).

**Data Availability Statement:** The original contributions presented in the study are included in the article, further inquiries can be directed to the corresponding author.

**Conflicts of Interest:** The authors declare no conflicts of interest.

## References

- Chakraborty, D.; Tirumala, T.; Chitral, S.; Sahoo, B.N.; Kiran, D.V.; Kumar, P.A. The State of the Art for Wire Arc Additive Manufacturing Process of Titanium Alloys for Aerospace Applications. *J. Mater. Eng. Perform.* **2022**, *31*, 6149–6182. [\[CrossRef\]](#)
- Cunningham, C.R.; Flynn, J.M.; Shokrani, A.; Dhokia, V.; Newman, S.T. Invited Review Article: Strategies and Processes for High Quality Wire Arc Additive Manufacturing. *Addit. Manuf.* **2018**, *22*, 672–686. [\[CrossRef\]](#)
- IvánTabernero; Paskual, A.; Álvarez, P.; Suárez, A. Study on Arc Welding Processes for High Deposition Rate Additive Manufacturing. *Procedia CIRP* **2018**, *68*, 358–362. [\[CrossRef\]](#)
- Sharma, S.K.; Maheshwari, S. Arc Characterization Study for Submerged Arc Welding of HSLA (API X80) Steel. *J. Mech. Sci. Technol.* **2017**, *31*, 1383–1390. [\[CrossRef\]](#)
- Dinovitzer, M.; Chen, X.; Laliberte, J.; Huang, X.; Frei, H. Effect of Wire and Arc Additive Manufacturing (WAAM) Process Parameters on Bead Geometry and Microstructure. *Addit. Manuf.* **2019**, *26*, 138–146. [\[CrossRef\]](#)
- Papacharalampopoulos, A.; Sabatakakis, K.; Stavropoulos, P. Quality Monitoring of RSW Processes. The Impact of Vibrations. *Procedia CIRP* **2023**, *118*, 895–900. [\[CrossRef\]](#)
- Gurmesa, F.D.; Lemu, H.G. Literature Review on Thermomechanical Modelling and Analysis of Residual Stress Effects in Wire Arc Additive Manufacturing. *Metals* **2023**, *13*, 526. [\[CrossRef\]](#)
- Jafari, D.; Vaneker, T.H.J.; Gibson, I. Wire and Arc Additive Manufacturing: Opportunities and Challenges to Control the Quality and Accuracy of Manufactured Parts. *Mater. Des.* **2021**, *202*, 109471. [\[CrossRef\]](#)
- Karlina, A.I.; Karlina, Y.I.; Kondratiev, V.V.; Kononenko, R.V.; Breki, A.D. Study of Wear of an Alloyed Layer with Chromium Carbide Particles after Plasma Melting. *Crystals* **2023**, *13*, 1696. [\[CrossRef\]](#)
- Sarathchandra, D.T.; Davidson, M.J.; Visvanathan, G. Parameters Effect on SS304 Beads Deposited by Wire Arc Additive Manufacturing. *Mater. Manuf. Process.* **2020**, *35*, 852–858. [\[CrossRef\]](#)
- Le, V.T.; Doan, Q.T.; Mai, D.S.; Bui, M.C.; Tran, H.S.; Van Tran, X.; Nguyen, V.A. Prediction and Optimization of Processing Parameters in Wire and Arc-Based Additively Manufacturing of 316L Stainless Steel. *J. Braz. Soc. Mech. Sci. Eng.* **2022**, *44*, 394. [\[CrossRef\]](#)
- Srivastava, S.; Garg, R.K.; Sharma, V.S.; Sachdeva, A. Measurement and Mitigation of Residual Stress in Wire-Arc Additive Manufacturing: A Review of Macro-Scale Continuum Modelling Approach. *Arch. Comput. Methods Eng.* **2021**, *28*, 3491–3515. [\[CrossRef\]](#)
- Geng, R.; Du, J.; Wei, Z.; Xu, S.; Ma, N. Modelling and Experimental Observation of the Deposition Geometry and Microstructure Evolution of Aluminum Alloy Fabricated by Wire-Arc Additive Manufacturing. *J. Manuf. Process.* **2021**, *64*, 369–378. [\[CrossRef\]](#)
- Hanif, M.; Shah, A.H.; Shah, I.; Mumtaz, J. Optimization of Bead Geometry during Tungsten Inert Gas Welding Using Grey Relational and Finite Element Analysis. *Materials* **2023**, *16*, 3732. [\[CrossRef\]](#) [\[PubMed\]](#)
- Sharma, R.; Raj Paul, A.; Mukherjee, M.; Ram Krishna Vadali, S.; Kumar Singh, R.; Kumar Sharma, A. Forecasting of Process Parameters Using Machine Learning Techniques for Wire Arc Additive Manufacturing Process. *Mater. Today Proc.* **2023**, *80*, 248–253. [\[CrossRef\]](#)
- Barrionuevo, G.O.; Sequeira-Almeida, P.M.; Ríos, S.; Ramos-Grez, J.A.; Williams, S.W. A machine learning approach for the prediction of melting efficiency in wire arc additive manufacturing. *Int. J. Adv. Manuf. Technol.* **2022**, *120*, 3123–3133. [\[CrossRef\]](#)
- Yaseer, A.; Chen, H. Machine Learning Based Layer Roughness Modeling in Robotic Additive Manufacturing. *J. Manuf. Process.* **2021**, *70*, 543–552. [\[CrossRef\]](#)
- Xia, C.; Pan, Z.; Polden, J.; Li, H.; Xu, Y.; Chen, S. Modelling and prediction of surface roughness in wire arc additive manufacturing using machine learning. *J. Intell. Manuf.* **2021**, *33*, 1467–1482. [\[CrossRef\]](#)
- Wang, Z.; Zimmer-Chevret, S.; Léonard, F.; Abba, G. Prediction of Bead Geometry with Consideration of Interlayer Temperature Effect for CMT-Based Wire-Arc Additive Manufacturing. *Weld. World* **2021**, *65*, 2255–2266. [\[CrossRef\]](#)

20. Lee, S.H. Optimization of Cold Metal Transfer-Based Wire Arc Additive Manufacturing Processes Using Gaussian Process Regression. *Metals* **2020**, *10*, 461. [[CrossRef](#)]
21. Yadav, A.; Srivastava, M.; Jain, P.K.; Rathee, S. Investigation of Bead Morphology and Mechanical Behaviour for Metal Inert Gas Welding-Based WAAM in Pulsed Mode Metal Transfer on 316LSi Stainless Steel. *J. Adhes. Sci. Technol.* **2024**, *38*, 738–769. [[CrossRef](#)]
22. Oh, W.-J.; Lee, C.-M.; Kim, D.-H. Prediction of Deposition Bead Geometry in Wire Arc Additive Manufacturing Using Machine Learning. *J. Mater. Res. Technol.* **2022**, *20*, 4283–4296. [[CrossRef](#)]
23. Xia, C.; Pan, Z.; Polden, J.; Li, H.; Xu, Y.; Chen, S.; Zhang, Y. A Review on Wire Arc Additive Manufacturing: Monitoring, Control and a Framework of Automated System. *J. Manuf. Syst.* **2020**, *57*, 31–45. [[CrossRef](#)]
24. Venkata Rao, K.; Parimi, S.; Suvarna Raju, L.; Suresh, G. Modelling and Optimization of Weld Bead Geometry in Robotic Gas Metal Arc-Based Additive Manufacturing Using Machine Learning, Finite-Element Modelling and Graph Theory and Matrix Approach. *Soft Comput.* **2022**, *26*, 3385–3399. [[CrossRef](#)]
25. Karmuhilan, M.; Sood, A.K. Intelligent Process Model for Bead Geometry Prediction in WAAM. *Mater. Today Proc.* **2018**, *5*, 24005–24013. [[CrossRef](#)]
26. Hu, Z.; Qin, X.; Li, Y.; Ni, M. Welding Parameters Prediction for Arbitrary Layer Height in Robotic Wire and Arc Additive Manufacturing. *J. Mech. Sci. Technol.* **2020**, *34*, 1683–1695. [[CrossRef](#)]
27. Yuan, L.; Pan, Z.; Ding, D.; He, F.; Van Duin, S.; Li, H.; Li, W. Investigation of Humping Phenomenon for the Multi-Directional Robotic Wire and Arc Additive Manufacturing. *Robot. Comput. -Integr. Manuf.* **2020**, *63*, 101916. [[CrossRef](#)]
28. Yildiz, A.S.; Davut, K.; Koc, B.; Yilmaz, O. Wire arc additive manufacturing of high-strength low alloy steels: Study of process parameters and their influence on the bead geometry and mechanical characteristics. *Int. J. Adv. Manuf. Technol.* **2020**, *108*, 3391–3404. [[CrossRef](#)]
29. Chen, C.; He, H.; Zhou, J.; Lian, G.; Huang, X.; Feng, M. A Profile Transformation Based Recursive Multi-Bead Overlapping Model for Robotic Wire and Arc Additive Manufacturing (WAAM). *J. Manuf. Process.* **2022**, *84*, 886–901. [[CrossRef](#)]
30. Ding, D.; Pan, Z.; Cuiuri, D.; Li, H. A Multi-Bead Overlapping Model for Robotic Wire and Arc Additive Manufacturing (WAAM). *Robot. Comput. -Integr. Manuf.* **2015**, *31*, 101–110. [[CrossRef](#)]
31. Chen, C.; He, H.; Zhou, S.; Lian, G.; Huang, X.; Feng, M. Prediction of Multi-Bead Profile of Robotic Wire and Arc Additive Manufactured Components Recursively Using Axisymmetric Drop Shape Analysis. *Virtual Phys. Prototyp.* **2023**, *18*, e2254563. [[CrossRef](#)]
32. Lambiase, F.; Scipioni, S.I.; Paoletti, A. Accurate Prediction of the Bead Geometry in Wire Arc Additive Manufacturing Process. *Int. J. Adv. Manuf. Technol.* **2022**, *119*, 7629–7639. [[CrossRef](#)]
33. Zhao, Y.; Li, F.; Chen, S.; Lu, Z. Unit Block-Based Process Planning Strategy of WAAM for Complex Shell-Shaped Component. *Int. J. Adv. Manuf. Technol.* **2019**, *104*, 3915–3927. [[CrossRef](#)]
34. Castro-Neto, M.; Jeong, Y.-S.; Jeong, M.-K.; Han, L.D. Online-SVR for Short-Term Traffic Flow Prediction under Typical and Atypical Traffic Conditions. *Expert Syst. Appl.* **2009**, *36*, 6164–6173. [[CrossRef](#)]
35. Chen, T.; He, T.; Benesty, M.; Khotilovich, V.; Tang, Y.; Cho, H. Xgboost: Extreme gradient boosting. *R Package Version 0.4–2* **2015**, *1*, 1–4.
36. Hecht-Nielsen, R. Theory of the backpropagation neural network. In Proceedings of the International Joint Conference on Neural Networks, Washington, DC, USA, 18–22 June 1989; Volume 1, pp. 593–605.
37. Nawi, N.M.; Khan, A.; Rehman, M.Z. A New Back-Propagation Neural Network Optimized with Cuckoo Search Algorithm. In *Computational Science and Its Applications—ICCSA 2013: 13th International Conference, Ho Chi Minh City, Vietnam, 24–27 June 2013*; Lecture Notes in Computer Science; Murgante, B., Misra, S., Carlini, M., Torre, C.M., Nguyen, H.-Q., Taniar, D., Apduhan, B.O., Gervasi, O., Eds.; Springer: Berlin/Heidelberg, Germany, 2013; Volume 7971, pp. 413–426. ISBN 978-3-642-39636-6.
38. Anandan, B.; Manikandan, M. Machine Learning Approach with Various Regression Models for Predicting the Ultimate Tensile Strength of the Friction Stir Welded AA 2050-T8 Joints by the K-Fold Cross-Validation Method. *Mater. Today Commun.* **2023**, *34*, 105286. [[CrossRef](#)]
39. Yu, T.; Zhu, H. Hyper-parameter optimization: A review of algorithms and applications. *arXiv* **2020**, arXiv:2003.05689.

**Disclaimer/Publisher’s Note:** The statements, opinions and data contained in all publications are solely those of the individual author(s) and contributor(s) and not of MDPI and/or the editor(s). MDPI and/or the editor(s) disclaim responsibility for any injury to people or property resulting from any ideas, methods, instructions or products referred to in the content.